arXiv:2007.03778v2 [cs.CV] 2 Nov 2020

3D Shape Reconstruction from Vision and Touch

Edward J. Smith[1,2*] **Roberto Calandra**[1] **Adriana Romero**[1,2] **Georgia Gkioxari**[1]

David Meger[2] **Jitendra Malik**[1,3] **Michal Drozdzal**[1]

[1] Facebook AI Research [2] McGill University [3] University of California, Berkeley

Abstract

When a toddler is presented a new toy, their instinctual behaviour is to pick it up and inspect it with their hand and eyes in tandem, clearly searching over its surface to properly understand what they are playing with. At any instance here, touch provides high fidelity localized information while vision provides complementary global context. However, in 3D shape reconstruction, the *complementary* fusion of visual and haptic modalities remains largely unexplored. In this paper, we study this problem and present an effective chart-based approach to multi-modal shape understanding which encourages a similar fusion vision and touch information. To do so, we introduce a dataset of simulated touch and vision signals from the interaction between a robotic hand and a large array of 3D objects. Our results show that (1) leveraging both vision and touch signals consistently improves single-modality baselines; (2) our approach outperforms alternative modality fusion methods and strongly benefits from the proposed chart-based structure; (3) the reconstruction quality increases with the number of grasps provided; and (4) the touch information not only enhances the reconstruction at the touch site but also extrapolates to its local neighborhood.

1 Introduction

From an early age children clearly and often loudly demonstrate that they need to both look and touch any new object that has peaked their interest. The instinctual behavior of inspecting with both their eyes and hands in tandem demonstrates the importance of fusing vision and touch information for 3D object understanding. Through machine learning techniques, 3D models of both objects and environments have been built by independent leveraging a variety of perception-based sensors, such as those for vision (e.g. a single RGB image) [59, 19] and touch [74, 68]. However, vision and touch possess a clear complementary nature. On one hand, vision provides a global context for object understanding, but is hindered by occlusions introduced by the object itself and from other objects in the scene. Moreover, vision is also affected by bas-relief [40] and scale/distance ambiguities, as well as slant/tilt angles [3]. On the other hand, touch provides localized 3D shape information, including the point of contact in space as well as high spatial resolution of the shape, but fails quickly when extrapolating without global context or strong priors. Hence, combining both modalities should lead to richer information and better models for 3D understanding. An overview of 3D shape reconstruction from vision and touch is displayed in Figure 1.

Visual and haptic modalities have been combined in the literature [2] to learn multi-modal representations of the 3D world, and improve upon subsequent 3D understanding tasks such as object manipulation [42] or any-modal conditional generation [43]. Tactile information has also been used

*Correspondence to: ejsmith@fb.com and edward.smith@mail.mcgill.ca

34th Conference on Neural Information Processing Systems (NeurIPS 2020), Vancouver, Canada.

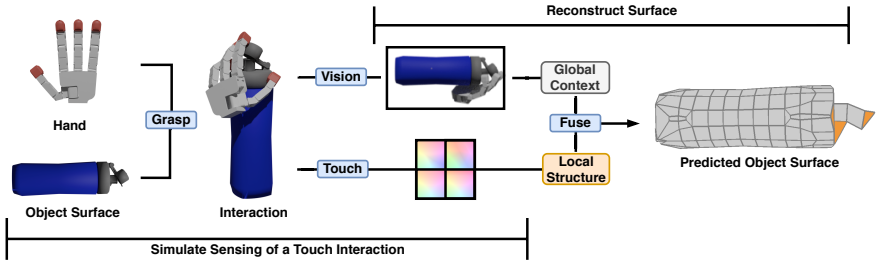


Figure 1: 3D shape understanding from vision and touch includes: (1) shape sensing with a camera and touch sensor, as well as (2) reconstruction algorithm that fuses vision and touch readings. In this paper, we introduce a dataset that captures object sensing and propose a chart-based fusion model for 3D shape prediction from multi-modal inputs. For touch, we realistically simulate an existing vision-based tactile sensor [41].

to improve 3D reconstructions in real environments. In particular, [68] leverages vision and touch sequentially, by first using vision to learn 3D object shape priors on simulated data, and subsequently using touch to refine the vision reconstructions when performing sim2real transfer. However, to the best of our knowledge, the *complementary* fusion of vision (in particular, RGB images) and touch in 3D shape reconstruction remains largely unexplored.

In this paper, we focus on this unexplored space, and present an approach that effectively fuses the global and local information provided by visual and haptic modalities to perform 3D shape reconstruction. Inspired by the papier-mâché technique of AtlasNet and its similar works [21, 73, 14] and leveraging recent advances in graph convolutional networks (GCN) [39], we aim to represent a 3D object with a collection of disjoint mesh surface elements, called *charts* [33], where some charts are reserved for tactile signals and others are used to represent visual information. More precisely, given an RGB image of an object and high spatial resolution tactile (mimicking a DIGIT tactile sensor [41]) and pose information of a grasp, the approach predicts a high fidelity local chart at each touch site and then uses the corresponding vision information to predict global charts which close the surface around them, in a fill-in-the-blank type procedure. As learning from real world robot interactions is resource and time intensive, we have designed a simulator to produce a multi-modal dataset of interactions between a robotic hand and four classes of objects, that can be used to benchmark approaches to 3D shape reconstructions from vision and touch, and help advance the field. Our dataset contains ground truth 3D objects as well as recordings from vision and tactile sensors, such as RGB images and touch readings. Results on the proposed dataset show that by combining visual and tactile cues, we are able to outperform single modality touch and vision baselines. We demonstrate the intuitive property that learning from touch exclusively translates into decreased performance, as the 3D shape reconstruction suffers from poor global context while learning from vision exclusively suffers from occlusions and leads to lower local reconstruction accuracy. However, when combining both modalities, we observe a systematic improvement, suggesting that the proposed approach effectively benefits from vision and touch signals, and surpasses alternative fusion strategies. Moreover, when increasing the number of grasps provided, we are able to further boost the 3D shape reconstruction quality. Finally, due to our model design, the touch readings not only enhance the reconstruction at the touch site but also reduce the error in the neighborhood of touch sensor position. Our main contributions can be summarized as: (1) we introduce a chart-based approach to 3D object reconstruction, leveraging GCNs to combine visual and haptic signals; (2) we build a dataset of simulated haptic object interactions to benchmark 3D shape reconstructions algorithms in this setting; and (3) through an extensive evaluation, we highlight the benefits of the proposed approach, which effectively exploits the complementarity of both modalities. Code for our system is publicly available on a GitHub repository, to ensure reproducible experimental comparison.[2]

2 Related Work

3D reconstruction from vision. There is a vast literature addressing 3D shape reconstruction from visual signals. Approaches often differ in their input visual signal – e.g. single view RGB image [60, 59, 19, 47], multi-view RGB images [12, 27, 35, 37], and depth images [55, 75] –, and their

[2]https://github.com/facebookresearch/3D-Vision-and-Touch

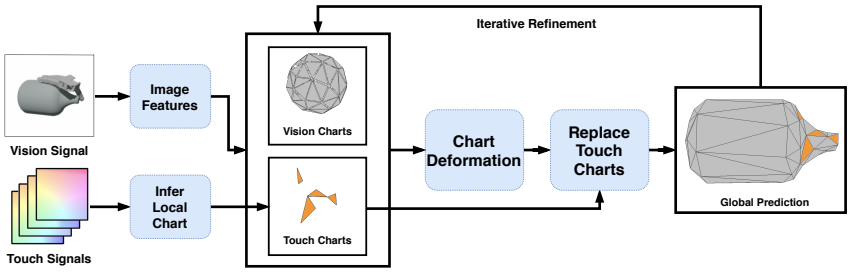


Figure 2: Our approach to 3D shape reconstruction combines a single RGB image with 4 touch readings. We start by predicting touch charts from a touch recordings, and projecting the visual signal onto all charts. Then, we feed the charts into an iterative deformation process, where we enforce touch consistency. As a result, we obtain a global prediction of deformed charts.

predicted 3D representation – e.g., orientation/3D pose [26, 17], signed distance functions [46], voxels, point clouds, and meshes [32]. Point cloud-based approaches [16, 53, 29, 48], together with voxel-based approaches [9, 60, 64, 70–72], and their computationally efficient counter-parts [54, 63, 23] have long dominated the deep learning-based 3D reconstruction literature. However, recent advances in graph neural networks [7, 13, 39, 66, 22] have enabled the effective processing and increasing use of surface meshes [36, 67, 34, 30, 25, 59, 8] and hybrid representations [20, 19]. While more complex in their encoding, mesh-based representations benefit greatly from their arbitrary resolution over other more naive representations. Our chosen representation more closely relates to the one of [20], which combines deformed sheets of points to form 3D shapes. However, unlike [20], our proposed approach exploits the neighborhood connectivity of meshes. Finally, 3D reconstruction has also been posed as a shape completion problem [60, 75], where the input is a partial point cloud obtained from depth information and the prediction is the complete version of it.

3D reconstruction from touch. Haptic signals have been exploited to address the shape completion problem [4, 51, 61, 49, 44]. Shape reconstruction has also been tackled from an active acquisition perspective, where successive touches are used to improve the reconstruction outcome and/or reduce the reconstruction uncertainty [5, 45, 74, 31, 15]. Most of these works use point-wise tactile sensors, while in contrast we use a high-dimensional and high-resolution sensor [41] which provide far more detailed local geometry with respect to the object being touched. In addition, these works make use only of proprioceptive and touch information, while we also tackle the problem of integrating global information from visual inputs in a principled manner. For an extensive and more general review on robotic tactile perception, we refer the reader to [44].

3D reconstruction from vision and touch. Many approaches exploiting vision and touch for 3D shape reconstruction rely on depth information [6, 28, 18]. In these works the depth information is represented as a sparse point cloud, augmented with touch points, which is fed to a Gaussian Process to predict implicit shape descriptors (e.g., level sets). Another line of work [68] considers RGB visual signals and uses a deep learning-based approach to produce voxelized 3D shape priors, which are subsequently refined with touch information when transferring the set-up to a real environment. Note that, following 3D shape reconstruction from touch, the previous works are concerned with the active acquisition of grasps. Moreover, [69] uses touch and partial depth maps separately to predict independent voxel models, which are then combined to produce a final prediction. In contrast to these works, we use a 4-fingered robot hand equipped with high-resolution tactile sensors – integrating such high-dimensional inputs is significantly more challenging but also potentially more useful for down-stream robot manipulation tasks.

3 Global and Local Reconstruction Methods

We consider the problem of 3D shape reconstruction from visual and haptic signals and leverage a deep learning approach which deforms disjoint mesh surface elements through a GCN. We assume that visual information is obtained from a single RGB image and haptic information is obtained from vision-based touch sensors with high spatial resolution, such as DIGIT [41]. More precisely, let V denote the RGB image used a as vision signal. Let $T = [R_i, P_i, M_i]_{i=1}^{n_t}$ denote the touch information, where R_i is one touch sensor reading, P_i its corresponding position and rotation in space, M_i a binary

mask indicating whether the touch is successful (i.e. the sensor is in contact with the object), and n_t is the number of touch sensors. Let O be the target object shape, represented as a surface mesh. The objective is to learn a function f_θ parameterized by θ that predicts an object shape reconstruction $\hat{O} = f_\theta(V, T)$ such that it best captures the surface defined by O. In our approach, we represent $\hat{O}$ as a set of independent surface elements, $\{C_i\}_{i=1}^{n_c}$, which we call *charts*. A chart, C_i, is implemented as a planar, 3D polygon mesh, composed of connected triangular faces, each defined by 3 vertex positions. Figure 3 depicts the structure of a chart, and outlines how a set of charts can be combined to form a closed 3D surface. In the left image we show how how a chart is parameterized by a simple planar mesh sheet, in the middle image, a collection of these charts, and in the right image how this collection is combined to form an atlas whose surface emulates that of a pyramid. The decomposition of the surface into charts allows us to have *vision-dedicated* and *touch-dedicated* charts, which we fuse by deforming the vision charts around the touch charts.

An overview of our approach is highlighted in Figure 2. Touch signals are used to predict *touch charts* using a pre-trained fully convolutional network, while vision signals are used to define image features over the set of *touch and vision charts* using perceptual feature pooling [67]. This set of vision and touch charts are then iteratively deformed to obtain the 3D shape reconstruction.

3.1 Merging vision and touch through chart deformation and tactile consistency

We adapt the mesh deformation setup outlined in [67, 59] and employ a GCN to deform our set of vision and touch charts. The GCN learns a function $f_{\theta_1}^{chart}$ parameterized by $\theta_1 \subset \theta$ that predicts the *residual* position of the vertices within each chart C_i through successive layers. Given a vertex u, each layer l of the GCN updates the vertex's features H_u^{l-1} as:

$$H_u^l = \sigma\left(W^l\left(\sum_{v \in \mathcal{N}_u \cup \{u\}} \frac{H_v^{l-1}}{\sqrt{|\mathcal{N}_u + 1||\mathcal{N}_v + 1|}}\right) + b^l\right), \tag{1}$$

where W^l and b^l are the learnable weights and biases of the l-the layer, σ is a non-linearity, and $\mathcal{N}_u$ are the neighbors of the vertex u. We initialize each vertex's features H_u^0 by concatenating vision features obtained by applying perceptual pooling to the input image, with the (x, y, z) position of the vertex in space, and a binary feature indicating whether the vertex is within a successful touch chart. The function $f_{\theta_1}^{chart}$ is trained to minimize the Chamfer Distance [62] between two sets of points S and $\hat{S}$ sampled from O and $\{C_i\}_{i=1}^{n_c}$, respectively, over a dataset $\mathcal{D}$:

$$\sum_{i \in \mathcal{D}}\left(\sum_{p \in S^{(i)}} \min_{\hat{p} \in \hat{S}^{(i)}} \|p - \hat{p}\|_2^2 + \sum_{\hat{p} \in \hat{S}^{(i)}} \min_{p \in S^{(i)}} \|p - \hat{p}\|_2^2\right). \tag{2}$$

GCNs enforce the exchange of information between vertices, which belong to the same neighborhood at every layer to allow information to propagate throughout the graph (see Figure 4a). Vertices in independent charts, however, will never lie in the same neighborhood, and so no exchange of information between charts can occur. To allow for the exchange of information between *vision* charts, we initially arrange the vision charts $\{C_i^v\}_{i=1}^{n_{cv}}$ to form a closed sphere (with no chart overlap). Then, we update each vertex's neighborhood such that vertices on the boundaries of different charts are in each other's neighborhood if they initially touch (see Figure 4b). With this setup, the charts are able to effectively communicate throughout the deformation process, and move freely during the optimization to optimally emulate the target surface. This is advantageous over the standard mesh deformation scheme, which deforms an initial closed mesh, as the prediction is no longer constrained to any fixed surface genus. Moreover, to define the communication between *vision and touch* charts, and enable the touch charts to influence the position of the vision charts, a reference vertex from the center of each touch chart is elected to lie within the neighborhood of all boundary vertices of vision charts and vice versa (see Figure 4c). With this setup, every vision chart can communicate with other nearby vision charts, as well as the touch charts. This communication scheme allows local touch, and vision information to propagate and fuse over all charts.

The chart deformation occurs three times to refine the prediction [67, 59], with the predicted charts being fed back to the input of the GCN before producing a final prediction. In total, 95 vision charts are employed, each possessing 19 vertices and 24 faces each. Touch charts each posses 81 vertices and 128 faces. The GCN updates the positions of the charts, however the initial position of touch charts is enforced after every deformation step and in the final mesh, as their shape is known to be

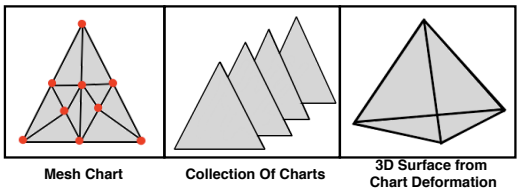


Figure 3: Structure of a chart along with how collections of charts can be deformed to produce a 3D surface, with vertices highlighted in red.

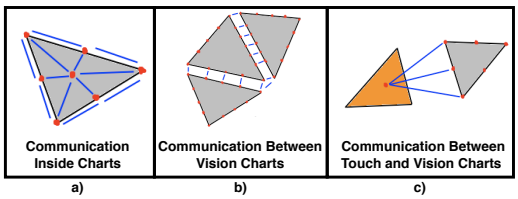


Figure 4: Communication within and between charts, with vertices highlighted in red, and communication between them highlighted in blue.

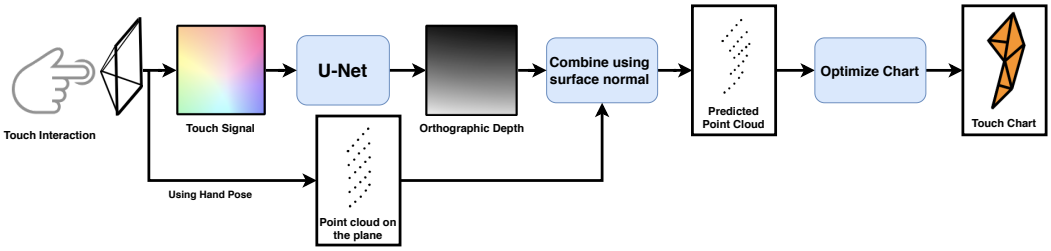


Figure 5: The pipeline for touch chart prediction from simulated touch readings. We start by predicting orthographic depth from touch reading image, then we combine orthographic depth with a point cloud sampled from the sensor plane using surface normal and obtain a predicted point cloud of local surface. To convert the predicted point cloud to touch chart by running an iterative optimization.

practically perfect. In this manner, the touch charts are fixed, and the vision charts learn to fill in the remaining surface around them through communication in the GCN. Touch charts corresponding to unsuccessful touches are initialized with simply the position of their finger tips at all vertices. This informs the model about where the fingers are in space, and so also where the object cannot be. Note that the position of unsuccessful touches is not enforced after their deformation.

3.2 Prediction of local touch charts

In this subsection, we describe how to obtain touch charts from touch signals produced using a gel-based sensor with high spatial resolution, such as the DIGIT [41]. To do this, we make note of what gel-based touch sensors truly observe: the impression of a surface through the gel. When untouched, the gel is lying perpendicular to the camera's perspective and at a fixed distance away. When touched by an object, that object's local surface is interpretable by the depth of the impression it makes across the plane of the gel. If we then want to recover this surface from the sensor, we simply need to interpret the touch signal in terms of the depth of the impression across this plane.

Figure 5 depicts the pipeline for local structure prediction. Using the finger position information P, we start by defining a grid of points $G_{init} \in \mathbb{R}^{100\times100\times3}$ of the same size and resolution as the sensor, lying on a perpendicular plane above it, which corresponds physically to the untouched gel of the sensor. Then, we apply a function $f^{touch}_{\theta_2}$, parameterized by $\theta_2 \subset \theta$, and represented as a fully convolutional network (U-Net-like model [56]) that takes as input the touch reading signal $R \in \mathbb{R}^{100\times100\times3}$ and predicts orthographic distance from each point to the surface [58]. This distance corresponds to the depth of the impression across the surface. Next, we transform this prediction into a point cloud $\hat{G}$ as:

$$\hat{G} = G_{init} + f^{touch}_{\theta_2}(R) * \hat{n}\,, \tag{3}$$

where $\hat{n}$ denotes the plane's unit normal. This transforms the grid of points to the shape of the gel across the impression, and so should match the local geometry which deformed it. To learn θ_2, we minimize the Chamfer distance between the predicted point cloud $\hat{G}$ and the ground truth point cloud local to the touch site, G. After predicting the local point cloud $\hat{G}$, a local touch chart C can be obtained by minimizing the Chamfer distance between points sampled from C and $\hat{G}$.

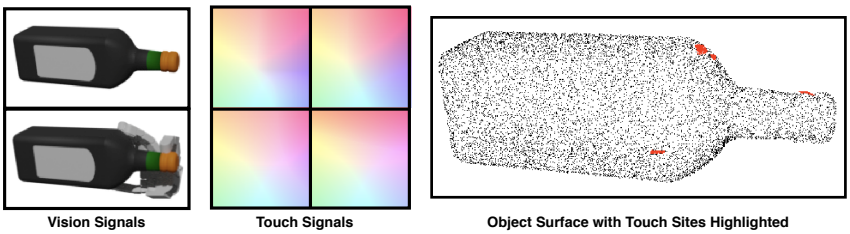


Figure 6: A data point from our dataset displaying an occluded (by hand) and unoccluded RGB image, 4 RGB images representing touch readings and a 3D object surface with touch sites highlighted.

4 A Visuotactile Dataset of Object-Grasp Interactions

To validate the model described in Section 3, we built a new dataset that aims to capture the interactions between a robotic hand and an object it is touching. We simulate these interactions using a Wonik's Allegro Hand [57] equipped with vision-based touch sensors [41] on each of its three fingers and thumb. We use objects from the 3D Warehouse [1], given its ubiquitous use in computer vision research, and to enable comparisons with previous vision-only work [59, 19, 21, 67].

An example instance of data collected from a single grasp is highlighted in Figure 6. We load example objects into the 3D robotics simulator Pybullet [11], place the hand randomly on its surface, and close its fingers attempting to produce contact between the sensors and some point on the object using inverse kinematics. To simulate the touch signal from each sensor, a grid of 10,000 points on the surface of the sensor are projected towards the object using sphere tracing [24] in Pytorch [50], defining a depth map from the sensor's perspective. We then define three lights (pure red, green and blue) around the boundary of the surface the depth map defines and a camera looking down at the surface from above. With this setup we then use the Phong reflection model [52] reflection model to compute the resulting simulated touch signal with resolution $100 \times 100 \times 3$. This process provides a quality approximation of how vision-based tactile sensors work and upon visual inspections the simulated images look plausible to a human expert. To acquire visual information from this interaction two images are rendered using Blender [10]: (1) a pre-interaction image of the object alone, and (2) an interaction image of an object occluded by the hand grasping it. Both images have resolution $256 \times 256 \times 3$ .Details with respect to the Allegro Hand, how the grasp simulations are performed in Pybullet, the rendering and scene settings in Blender, and the simulation of touch signals can be found in the supplemental materials.

The bottle, knife, cellphone, and rifle were chosen from the 3D Warehouse data due to their hand-held nature for a total of 1732 objects. From each grasp an occluded image, an unoccluded image, four simulated touch signals with a mask indicating if each touch was successful, the hand's current pose, a global point cloud of the object's shape, and four local point clouds defining each touch site are recorded. This information is visualized in Figure 6. From each object, five hand-object interactions, or grasps are recorded, and for each grasps at least one successful touch occurs, though on average 62.4% of touches are successful. We split the dataset into training and test sets with approximately a 90:10 ratio. Further details on the design and content of this dataset, together with in-depth statistics and analysis of the content, are provided in the supplemental materials.

5 Experimental Results

In the following section, we describe the experiments designed to validate our approach to 3D reconstruction that leverages both visual and haptic sensory information. We start by outlining our model selection process. Then, using our best model, we validate generalization of the complementary role of vision and touch for 3D shape reconstruction. We follow by examining the effect of increasing number of grasps and then measure the ability of our approach to effectively extrapolate around touch sites. For all experiments, details with respect to experiment design, optimization procedures, hardware used, runtime, and hyper-parameters considered can be found in the supplemental materials.

5.1 Complementarity of vision and touch: model selection and generalization

In the model selection, we compare our approach to three other modality fusion strategies on the validation set: (1) **Sphere-based**, where the chart-based initialization is replaced with a sphere-based

Row	Model	Vision	Touch	Bottle	Knife	Cellphone	Rifle	Average
1	Sphere-based	U	✓	0.775	0.572	1.262	0.643	0.813
2	Chart-based (no copying)	U	✓	0.741	**0.538**	1.141	0.603	0.756
3	Chart-based (no comm.)	U	✓	**0.709**	0.723	1.222	0.500	0.788
4	Ours	U	✓	0.741	0.676	**1.116**	**0.473**	**0.751**
5	Sphere-based	O	✓	0.985	0.692	1.270	1.023	0.992
6	Chart-based (no copying)	O	✓	0.953	**0.656**	1.176	0.892	0.919
7	Chart-based (no comm.)	O	✓	0.954	0.784	1.413	0.904	1.014
8	Ours	O	✓	**0.872**	0.685	**1.142**	**0.806**	**0.876**
9	Sphere-based	U	✗	0.816	**0.561**	1.322	0.667	0.841
10	Ours	U	✗	**0.783**	0.703	**1.115**	**0.588**	**0.797**
11	Sphere-based	O	✗	1.093	**0.719**	1.404	1.074	1.072
12	Ours	O	✗	**0.994**	0.831	**1.301**	**0.956**	**1.020**

Table 1: Model selection. We report the per-class Chamfer distance for the validation set together with average value. Note that O stands for *occluded* and U for *unoccluded*

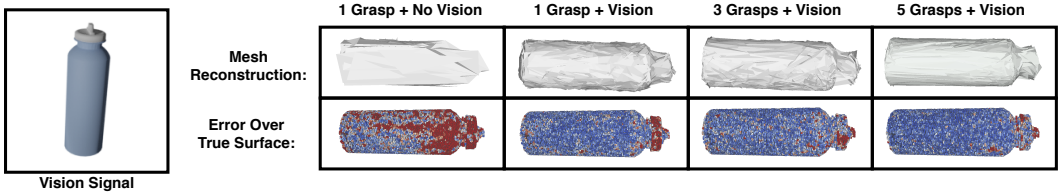


Figure 7: Reconstruction results of our method across different input modalities and number of grasps. For vision signal, we use an unoccluded RGB image.

one, and the sphere vertices contain a concatenation of projected vision features and touch features extracted from a simple CNN; (2) **Chart-based (no copying)**, where we remove the hard copying of local touch charts in the prediction; and (3) **Chart-based (no comm.)**, where we remove the communication between charts in the GCN and only copy them to the final prediction. For vision only inputs, we compare our model to the sphere-based model only. For all comparisons we consider both the occluded and unoccluded vision signals.

The results of model selection are presented in Table 1. We observe that: (1) the sphere-based model suffers from a decrease in average performance when compared to our model (see rows 1 vs 4, 5 vs 8, 9 vs 10, and 11, vs 12), (2) the copying of the local charts to the final prediction leads to performance boosts (see rows 2 vs 4, and 6 vs 8), and (3) the global prediction benefits from communication between touch and vision charts (see rows 3 vs 4, and 7 vs 8). Moreover, as expected, we notice a further decrease in average performance when comparing each unoccluded vision model with their occluded vision counterpart. Finally, for models leveraging vision and touch, we consistently observe an improvement w.r.t. their vision-only baselines, which particularly benefits our full chart-based approach. This improvement is especially noticeable when considering occluded vision, where touch information is able to enhance the reconstruction of sites occluded by the hand touching the object. To further validate our chart-based approach, its performance on single image 3D object reconstruction on [1] was evaluated and compared to an array of popular methods in this setting. The performance of our model here was highly competitive with that of state of the art methods and the results, details, and analysis of this experiment can be found in the supplemental materials.

In Table 2, we highlight the generalization of our best model by evaluating it on the test set for five 3D shape reconstruction set ups, namely occluded and unoccluded vision scenarios with and without touch. We notice that the improvement introduced by including the haptic modality generalizes to the test set, for both occluded and unoccluded vision signals. Moreover, we test our approach by removing the vision signal and optimizing it to recover the 3D shape using only tactile signals. In this case, we experience an increased global error of 3.050, compared to the next worse model with 1.074 error, demonstrating its difficulty to extrapolate without global context and further highlighting the locality of the touch signals. Finally, we display some example reconstructions that our best performing fusion models produce in Figure 7.

	Vision (occluded)		Vision (unoccluded)		
Input	Touch	No Touch	Touch	No touch	Touch only
Ours	0.991	1.074	0.804	0.861	3.050

Table 2: Test set results for 3D reconstruction tasks with different input modalities: combination of touch readings and occluded or unoccluded vision signal.

Class	Bottle	Knife	Cellphone	Rifle
C.D.	0.0099	0.0136	0.0072	0.00749

Table 3: Chamfer distance per class for local point cloud prediction at each touch site.

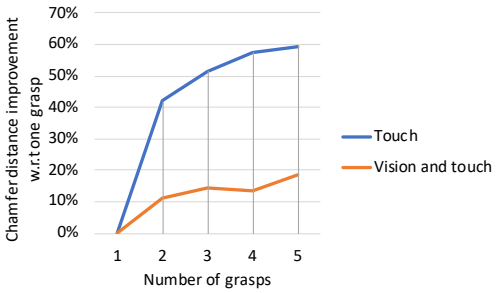


Figure 8: Multi-grasp experiment: we depict the Chamfer distance increase w.r.t. one grasp.

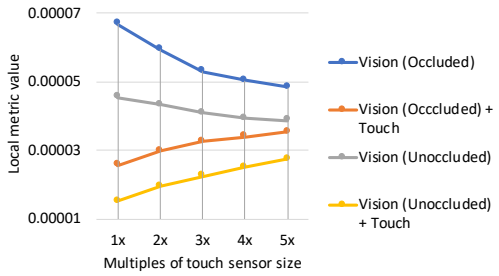


Figure 9: Local Chamfer distance at expanding distances around each touch site.

5.2 Going beyond a single grasp: Multi-grasp experiments

We design a further experiment in which we examine the effect of providing increasing number of grasps. The only practical change to the model here is that the number of touch charts increases by 4 for every additional grasp provided. This experiment is conducted using 1 to 5 grasps, and in both the touch-only setting where vision information is excluded and the unoccluded vision and touch setting. The results of this experiment are shown in Figure 8, where we demonstrate that by increasing the number of grasps provided, the reconstruction accuracy significantly improves both with and without the addition of unoccluded vision signals. Reconstruction results across different numbers of grasps can be viewed in Figure 7. From this experiment, it can be concluded that our model gains greater insight into the nature of an object by touching new areas on its surface.

5.3 From touch sensor readings to local structure prediction

Per-class reconstruction results at each touch site using the U-Net-based architecture are highlighted in Table 3. As expected, the reconstructions are practically perfect, when compared to the error incurred over full surfaces (smallest average global error of 0.804). The small errors incurred here are mainly due to the fact that predicted points are selected as belonging to the surface by observing differences in the touch signal and an untouched touch signal. This leads to overshooting and undershooting of the boundary of the touch, and consequently too large or too small predicted surfaces. A reconstruction result from this experiment is displayed in Figure 10.

Last, we design an experiment which examines how well the the target surface is reconstructed in expanding regions around each touch site. To do this, square rings of points of 1 to 5 times larger dimensions than the touch sensor are projected onto each object's surface at each touch site in order to produce increasingly distant regions around them. Then, the mean distance from these points to the closest point in the corresponding prediction is computed to determine how well these regions have been reconstructed. We perform this experiment with and without touch for both occluded and unoccluded vision models, and the results are shown in Figure 9. As expected, the vision-only models incur approximately the same loss at every plane size while models which leverage touch begin with a drastically lower loss and only slowly increase errors as the plane size increases. This experiment implies that the sharing of information between local and global charts allows for the propagation of touch information to regions around each touch site, suggesting a successful fusion of the complementary signals of vision and touch.

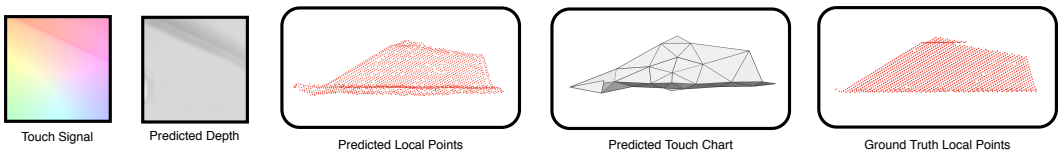


Figure 10: Local prediction of structure at a touch site, together with the touch chart.

5.4 Limitations

There exist a few limitations of this method which are worth addressing. The first noteworthy limitation is that in the final object predictions, charts sometimes poorly overlap creating a noisy boundary, as opposed to a more attractive smooth surface. This can be credited to the lack of natural regularizers for encouraging smoothness, which exist in more constrained methods [67, 59, 36]. This property can be observed in Figure 7. A second, and somewhat related limitation of the method is that charts are not forced to form a continuous connected surface. This occasionally leads to charts lying disconnected for the mainly body of the predicted surface. However, from our qualitative evaluation of 100 predicted objects in the test set, this only occurs 5% of the time, and has very little effect on the quality of the predictions. A final limitation is that our method requires full 3D scene information while training, and at test time requires full hand pose information. While trivial to acquire in our simulated environment, for application to real environments this data requirement is somewhat unrealistic.

6 Conclusion

In this paper, we explored the problem of 3D shape reconstruction from vision and touch. To do so, we introduced a dataset of simulated touch and vision signals, and proposed a chart-based approach that effectively exploits the complementary nature of both modalities, namely, the high fidelity local information from touch and the global information from vision. While some limitations to our approach exist such as potentially noisy or incomplete surface predictions, our results consistently highlight the benefit of combining both modalities to improve upon single modality baselines, and show the potential of using a chart-based approach to combine vision and touch signal in a principled way. The benefit of fusing vision and touch is further emphasized by the ability of our model to gracefully extrapolate around touch sites, and by the improved reconstruction accuracy when providing an increasing number of grasps, which suggests that the active sensing of visual and touch signals is a promising avenue to improve 3D shape reconstruction.

Broader Impact

Our contributions allows for improved understanding of the three dimensional world in which we all live. The impact of this work lies mainly in the field of 3D object understanding, such as better 3D reconstruction of objects in simulated environments as well as potential improvements in shape understanding in real world robot-object manipulation. There are many benefits to using improved 3D object understanding, and it may prove especially useful for the fields of automation, robotic, computer graphics and augmented and virtual reality. Failures of these models could arise if automation tools are not properly introduced, and biases are not properly addressed. In particular, these models could result in poor recognition of 3D objects in diverse contexts, as has already been shown for 2D recognition systems. On the research side, to mitigate these risks, we encourage further investigation to outline the performance of 3D understanding systems in the wild in a diverse set of contexts and geographical locations, and to mitigate the associated performance drops.

7 Acknowledgments

We would like to acknowledge the NSERC Canadian Robotics Network, the Natural Sciences and Engineering Research Council, and the Fonds de recherche du Québec – Nature et Technologies for their funding support, as granted to the McGill University authors. We would also like to thank Scott Fujimoto and Shaoxiong Wang for their helpful feedback.

References

[1] 3D Warehouse. `https://3dwarehouse.sketchup.com/`. Accessed: 2019-11-15.

[2] Peter Allen. Surface descriptions from vision and touch. In *IEEE International Conference on Robotics and Automation (ICRA)*, volume 1, pages 394–397. IEEE, 1984.

[3] P. N. Belhumeur, D. J. Kriegman, and A. L. Yuille. The bas-relief ambiguity. In *Proceedings of IEEE Computer Society Conference on Computer Vision and Pattern Recognition*, pages 1060–1066, 1997.

[4] A. Bierbaum, I. Gubarev, and R. Dillmann. Robust shape recovery for sparse contact location and normal data from haptic exploration. In *2008 IEEE/RSJ International Conference on Intelligent Robots and Systems (IROS)*, pages 3200–3205, 2008.

[5] Alexander Bierbaum, Matthias Rambow, Tamim Asfour, and Rudiger Dillmann. A potential field approach to dexterous tactile exploration of unknown objects. In *IEEE-RAS International Conference on Humanoid Robots (Humanoids)*, pages 360–366. IEEE, 2008.

[6] Mårten Björkman, Yasemin Bekiroglu, Virgile Högman, and Danica Kragic. Enhancing visual perception of shape through tactile glances. In *IEEE International Conference on Intelligent Robots and Systems (IROS)*, 11 2013.

[7] Joan Bruna, Wojciech Zaremba, Arthur Szlam, and Yann Lecun. Spectral networks and locally connected networks on graphs. In *International Conference on Learning Representations (ICLR)*, 2014.

[8] Wenzheng Chen, Huan Ling, Jun Gao, Edward Smith, Jaakko Lehtinen, Alec Jacobson, and Sanja Fidler. Learning to predict 3d objects with an interpolation-based differentiable renderer. In *Advances in Neural Information Processing Systems*, pages 9609–9619, 2019.

[9] Christopher B Choy, Danfei Xu, JunYoung Gwak, Kevin Chen, and Silvio Savarese. 3d-r2n2: A unified approach for single and multi-view 3d object reconstruction. In *Proceedings of the European Conference on Computer Vision (ECCV)*, pages 628–644. Springer, 2016.

[10] Blender Online Community. *Blender - a 3D modelling and rendering package*. Blender Foundation, Stichting Blender Foundation, Amsterdam, 2018.

[11] Erwin Coumans and Yunfei Bai. Pybullet, a python module for physics simulation for games, robotics and machine learning. *GitHub repository*, 2016.

[12] A. Dame, V. A. Prisacariu, C. Y. Ren, and I. Reid. Dense reconstruction using 3d object shape priors. In *2013 IEEE Conference on Computer Vision and Pattern Recognition (CVPR)*, pages 1288–1295, 2013.

[13] Michaël Defferrard, Xavier Bresson, and Pierre Vandergheynst. Convolutional neural networks on graphs with fast localized spectral filtering. In *Proceedings of the 30th International Conference on Neural Information Processing Systems*, NIPS'16, pages 3844–3852, USA, 2016. Curran Associates Inc.

[14] Theo Deprelle, Thibault Groueix, Matthew Fisher, Vladimir Kim, Bryan Russell, and Mathieu Aubry. Learning elementary structures for 3d shape generation and matching. In *Advances in Neural Information Processing Systems*, pages 7435–7445, 2019.

[15] Danny Driess, Peter Englert, and Marc Toussaint. Active learning with query paths for tactile object shape exploration. In *n IEEE/RSJ International Conference on Intelligent Robots and Systems (IROS)*, 2017.

[16] Haoqiang Fan, Hao Su, and Leonidas Guibas. A point set generation network for 3d object reconstruction from a single image. In *IEEE Conference on Computer Vision and Pattern Recognition (CVPR)*, volume 38, 2017.

[17] D. F. Fouhey, A. Gupta, and M. Hebert. Data-driven 3d primitives for single image understanding. In *2013 IEEE International Conference on Computer Vision (CVPR)*, pages 3392–3399, 2013.

[18] Gabriela Zarzar Gandler, Carl Henrik Ek, Mårten Björkman, Rustam Stolkin, and Yasemin Bekiroglu. Object shape estimation and modeling, based on sparse gaussian process implicit surfaces, combining visual data and tactile exploration. *Robotics and Autonomous Systems*, 126:103433, 2020.

[19] Georgia Gkioxari, Jitendra Malik, and Justin Johnson. Mesh r-cnn. *IEEE International Conference on Computer Vision (ICCV)*, 2019.

[20] Thibault Groueix, Matthew Fisher, Vladimir G Kim, Bryan C Russell, and Mathieu Aubry. 3d-coded: 3d correspondences by deep deformation. In *Proceedings of the European Conference on Computer Vision (ECCV)*, pages 230–246, 2018.

[21] Thibault Groueix, Matthew Fisher, Vladimir G Kim, Bryan C Russell, and Mathieu Aubry. A papier-mâché approach to learning 3d surface generation. In *Proceedings of the IEEE Conference on Computer Vision and Pattern Recognition (CVPR)*, pages 216–224, 2018.

[22] Will Hamilton, Zhitao Ying, and Jure Leskovec. Inductive representation learning on large graphs. In *Advances in Neural Information Processing Systems (NeurIPS)*, pages 1024–1034, 2017.

[23] Christian Häne, Shubham Tulsiani, and Jitendra Malik. Hierarchical surface prediction for 3d object reconstruction. *arXiv preprint arXiv:1704.00710*, 2017.

[24] John C Hart. Sphere tracing: A geometric method for the antialiased ray tracing of implicit surfaces. *The Visual Computer*, 12(10):527–545, 1996.

[25] Paul Henderson and Vittorio Ferrari. Learning to generate and reconstruct 3d meshes with only 2d supervision. *arXiv preprint arXiv:1807.09259*, 2018.

[26] D. Hoiem, A. A. Efros, and M. Hebert. Geometric context from a single image. In *IEEE International Conference on Computer Vision (ICCV)*, volume 1, pages 654–661 Vol. 1, 2005.

[27] C. Häne, N. Savinov, and M. Pollefeys. Class specific 3d object shape priors using surface normals. In *2014 IEEE Conference on Computer Vision and Pattern Recognition (CVPR)*, pages 652–659, 2014.

[28] Jarmo Ilonen, Jeannette Bohg, and Ville Kyrki. Three-dimensional object reconstruction of symmetric objects by fusing visual and tactile sensing. *The International Journal of Robotics Research*, 33(2):321–341, 2014.

[29] Eldar Insafutdinov and Alexey Dosovitskiy. Unsupervised learning of shape and pose with differentiable point clouds. *arXiv preprint arXiv:1810.09381*, 2018.

[30] Dominic Jack, Jhony K Pontes, Sridha Sridharan, Clinton Fookes, Sareh Shirazi, Frederic Maire, and Anders Eriksson. Learning free-form deformations for 3d object reconstruction. *arXiv preprint arXiv:1803.10932*, 2018.

[31] N. Jamali, C. Ciliberto, L. Rosasco, and L. Natale. Active perception: Building objects' models using tactile exploration. In *IEEE-RAS International Conference on Humanoid Robots (Humanoids)*, pages 179–185, Nov 2016.

[32] Krishna Murthy Jatavallabhula, Edward Smith, Jean-Francois Lafleche, Clement Fuji Tsang, Artem Rozantsev, Wenzheng Chen, and Tommy Xiang. Kaolin: A pytorch library for accelerating 3d deep learning research. *arXiv preprint arXiv:1911.05063*, 2019.

[33] Jürgen Jost. *Riemannian Geometry and Geometric Analysis*, page 1. Springer, sixth edition, 2011.

[34] Angjoo Kanazawa, Shubham Tulsiani, Alexei A Efros, and Jitendra Malik. Learning category-specific mesh reconstruction from image collections. *arXiv preprint arXiv:1803.07549*, 2018.

[35] Abhishek Kar, Christian Häne, and Jitendra Malik. Learning a multi-view stereo machine. In I. Guyon, U. V. Luxburg, S. Bengio, H. Wallach, R. Fergus, S. Vishwanathan, and R. Garnett, editors, *Advances in Neural Information Processing Systems (NeurIPS)*, pages 365–376. Curran Associates, Inc., 2017.

[36] Hiroharu Kato, Yoshitaka Ushiku, and Tatsuya Harada. Neural 3d mesh renderer. *arXiv preprint arXiv:1711.07566*, 2017.

[37] Alex Kendall, Hayk Martirosyan, Saumitro Dasgupta, and Peter Henry. End-to-end learning of geometry and context for deep stereo regression. In *IEEE International Conference on Computer Vision (ICCV)*, pages 66–75. IEEE Computer Society, 2017.

[38] Diederik P Kingma and Jimmy Ba. Adam: A method for stochastic optimization. *arXiv preprint arXiv:1412.6980*, 2014.

[39] Thomas N. Kipf and Max Welling. Semi-supervised classification with graph convolutional networks. In *Proceedings of the 5th International Conference on Learning Representations (ICLR)*, 2017.

[40] Jan Koenderink, Andrea Doorn, and Astrid Kappers. Surface perception in picture. *Percept. Psychophys.*, 52:487–496, 09 1992.

[41] Mike Lambeta, Po-Wei Chou, Stephen Tian, Brian Yang, Benjamin Maloon, Victoria Rose Most, Dave Stroud, Raymond Santos, Ahmad Byagowi, Gregg Kammerer, Dinesh Jayaraman, and Roberto Calandra. DIGIT: A novel design for a low-cost compact high-resolution tactile sensor with application to in-hand manipulation. *IEEE Robotics and Automation Letters (RA-L)*, 5(3):3838–3845, 2020.

[42] M. A. Lee, Y. Zhu, K. Srinivasan, P. Shah, S. Savarese, L. Fei-Fei, A. Garg, and J. Bohg. Making sense of vision and touch: Self-supervised learning of multimodal representations for contact-rich tasks. In *2019 International Conference on Robotics and Automation (ICRA)*, pages 8943–8950, 2019.

[43] Jae Hyun Lim, Pedro O. Pinheiro, Negar Rostamzadeh, Chris Pal, and Sungjin Ahn. Neural multisensory scene inference. In *Advances in Neural Information Processing Systems 32: Annual Conference on Neural Information Processing Systems 2019, NeurIPS 2019, 8-14 December 2019, Vancouver, BC, Canada*, pages 8994–9004, 2019.

[44] Shan Luo, Joao Bimbo, Ravinder Dahiya, and Hongbin Liu. Robotic Tactile Perception of Object Properties: A Review. *arXiv e-prints*, page arXiv:1711.03810, November 2017.

[45] Uriel Martinez-Hernandez, Tony Dodd, Lorenzo Natale, Giorgio Metta, Tony Prescott, and Nathan Lepora. Active contour following to explore object shape with robot touch. In *2013 World Haptics Conference, WHC 2013*, 04 2013.

[46] Lars Mescheder, Michael Oechsle, Michael Niemeyer, Sebastian Nowozin, and Andreas Geiger. Occupancy networks: Learning 3d reconstruction in function space. In *Proceedings IEEE Conf. on Computer Vision and Pattern Recognition (CVPR)*, 2019.

[47] J Krishna Murthy, GV Sai Krishna, Falak Chhaya, and K Madhava Krishna. Reconstructing vehicles from a single image: Shape priors for road scene understanding. In *2017 IEEE International Conference on Robotics and Automation (ICRA)*, pages 724–731. IEEE, 2017.

[48] David Novotny, Diane Larlus, and Andrea Vedaldi. Learning 3d object categories by looking around them. In *IEEE International Conference on Computer Vision (ICCV)*, pages 5228–5237. IEEE, 2017.

[49] Simon Ottenhaus, Martin Miller, David Schiebener, Nikolaus Vahrenkamp, and Tamim Asfour. Local implicit surface estimation for haptic exploration. In *IEEE-RAS International Conference on Humanoid Robots (Humanoids)*, pages 850–856, 11 2016.

[50] Adam Paszke, Sam Gross, Francisco Massa, Adam Lerer, James Bradbury, Gregory Chanan, Trevor Killeen, Zeming Lin, Natalia Gimelshein, Luca Antiga, Alban Desmaison, Andreas Kopf, Edward Yang, Zachary DeVito, Martin Raison, Alykhan Tejani, Sasank Chilamkurthy, Benoit Steiner, Lu Fang, Junjie Bai, and Soumith Chintala. Pytorch: An imperative style, high-performance deep learning library. In H. Wallach, H. Larochelle, A. Beygelzimer, F. d'Alché-Buc, E. Fox, and R. Garnett, editors, *Advances in Neural Information Processing Systems 32*, pages 8024–8035. Curran Associates, Inc., 2019.

[51] Z. Pezzementi, C. Reyda, and G. D. Hager. Object mapping, recognition, and localization from tactile geometry. In *2011 IEEE International Conference on Robotics and Automation*, pages 5942–5948, 2011.

[52] Bui Tuong Phong. Illumination for computer generated pictures. *Communications of the ACM*, 18(6):311–317, 1975.

[53] Charles R Qi, Hao Su, Kaichun Mo, and Leonidas J Guibas. Pointnet: Deep learning on point sets for 3d classification and segmentation. *IEEE Conference on Computer Vision and Pattern Recognition (CVPR)*, 1(2):4, 2017.

[54] Gernot Riegler, Ali Osman Ulusoy, and Andreas Geiger. Octnet: Learning deep 3d representations at high resolutions. In *IEEE Conference on Computer Vision and Pattern Recognition (CVPR)*, pages 6620–6629, 2017.

[55] J. Rock, T. Gupta, J. Thorsen, J. Gwak, D. Shin, and D. Hoiem. Completing 3d object shape from one depth image. In *2015 IEEE Conference on Computer Vision and Pattern Recognition (CVPR)*, pages 2484–2493, 2015.

[56] Olaf Ronneberger, Philipp Fischer, and Thomas Brox. U-net: Convolutional networks for biomedical image segmentation. In *International Conference on Medical image computing and computer-assisted intervention*, pages 234–241. Springer, 2015.

[57] SimLab. Allegro hand overview, 2016. [Online; accessed 25-May-2020].

[58] Edward J. Smith, Scott Fujimoto, and David Meger. Multi-view silhouette and depth decomposition for high resolution 3d object representation. In *Advances in Neural Information Processing Systems*, pages 6479–6489, 2018.

[59] Edward J. Smith, Scott Fujimoto, Adriana Romero, and David Meger. Geometrics: Exploiting geometric structure for graph-encoded objects. In Kamalika Chaudhuri and Ruslan Salakhutdinov, editors, *Proceedings of the 36th International Conference on Machine Learning, ICML 2019*, volume 97 of *Proceedings of Machine Learning Research*, pages 5866–5876. PMLR, 2019.

[60] Edward J Smith and David Meger. Improved adversarial systems for 3d object generation and reconstruction. In *Conference on Robot Learning (CoRL)*, pages 87–96, 2017.

[61] Nicolas Sommer, Miao Li, and Aude Billard. Bimanual compliant tactile exploration for grasping unknown objects. *Proceedings - IEEE International Conference on Robotics and Automation*, pages 6400–6407, 09 2014.

[62] Xingyuan Sun, Jiajun Wu, Xiuming Zhang, Zhoutong Zhang, Chengkai Zhang, Tianfan Xue, Joshua B. Tenenbaum, and William T. Freeman. Pix3d: Dataset and methods for single-image 3d shape modeling. *CoRR*, abs/1804.04610, 2018.

[63] Maxim Tatarchenko, Alexey Dosovitskiy, and Thomas Brox. Octree generating networks: Efficient convolutional architectures for high-resolution 3d outputs. In *IEEE Conference on Computer Vision and Pattern Recognition (CVPR)*, pages 2088–2096, 2017.

[64] Shubham Tulsiani, Tinghui Zhou, Alexei A Efros, and Jitendra Malik. Multi-view supervision for single-view reconstruction via differentiable ray consistency. In *IEEE Conference on Computer Vision and Pattern Recognition (CVPR)*, pages 209–217. IEEE, 2017.

[65] Dmitry Ulyanov, Andrea Vedaldi, and Victor Lempitsky. Instance normalization: The missing ingredient for fast stylization. *arXiv preprint arXiv:1607.08022*, 2016.

[66] Petar Veličković, Guillem Cucurull, Arantxa Casanova, Adriana Romero, Pietro Liò, and Yoshua Bengio. Graph Attention Networks. *International Conference on Learning Representations (ICLR)*, 2018.

[67] Nanyang Wang, Yinda Zhang, Zhuwen Li, Yanwei Fu, Wei Liu, and Yu-Gang Jiang. Pixel2mesh: Generating 3d mesh models from single rgb images. *arXiv preprint arXiv:1804.01654*, 2018.

[68] S. Wang, J. Wu, X. Sun, W. Yuan, W. T. Freeman, J. B. Tenenbaum, and E. H. Adelson. 3d shape perception from monocular vision, touch, and shape priors. In *IEEE/RSJ International Conference on Intelligent Robots and Systems (IROS)*, pages 1606–1613, Oct 2018.

[69] David Watkins-Valls, Jacob Varley, and Peter Allen. Multi-modal geometric learning for grasping and manipulation. In *2019 International Conference on Robotics and Automation (ICRA)*, pages 7339–7345. IEEE, 2019.

[70] Jiajun Wu, Yifan Wang, Tianfan Xue, Xingyuan Sun, William T Freeman, and Joshua B Tenenbaum. MarrNet: 3D Shape Reconstruction via 2.5D Sketches. In *Advances In Neural Information Processing Systems (NeurIPS)*, 2017.

[71] Jiajun Wu, Chengkai Zhang, Tianfan Xue, William T Freeman, and Joshua B Tenenbaum. Learning a probabilistic latent space of object shapes via 3d generative-adversarial modeling. In *Advances in Neural Information Processing Systems (NeurIPS)*, pages 82–90, 2016.

[72] Jiajun Wu, Chengkai Zhang, Xiuming Zhang, Zhoutong Zhang, William T Freeman, and Joshua B Tenenbaum. Learning shape priors for single-view 3d completion and reconstruction. In *Proceedings of the European Conference on Computer Vision (ECCV)*, pages 673–691. Springer, 2018.

[73] Yaoqing Yang, Chen Feng, Yiru Shen, and Dong Tian. Foldingnet: Point cloud auto-encoder via deep grid deformation. In *Proceedings of the IEEE Conference on Computer Vision and Pattern Recognition*, pages 206–215, 2018.

[74] Zhengkun Yi, Roberto Calandra, Filipe Fernandes Veiga, Herke van Hoof, Tucker Hermans, Yilei Zhang, and Jan Peters. Active tactile object exploration with Gaussian processes. In *IEEE/RSJ International Conference on Intelligent Robots and Systems (IROS)*, pages 4925–4930, 2016.

[75] Wentao Yuan, Tejas Khot, David Held, Christoph Mertz, and Martial Hebert. Pcn: Point completion network. In *2018 International Conference on 3D Vision (3DV)*, pages 728–737, 2018.

Supplemental Materials

In the following sections, we provide additional details with respect to various elements of the paper which could not be fully expanded upon in the main paper. This begins with an in depth explanation of the proposed dataset, including its exact contents, and the manner in which they were produced. This is followed by a closer look into the various aspects of touch chart prediction including architectures, experimental procedures, hyper-parameters, and additional results. Finally, a comprehensive examination of the prediction of vision charts is provided, again with detailed explanations of architectures, experimental procedures, hyper-parameters, and additional results.

A Visuotactile Dataset

This section describes the multi-modal dataset of simulated 3D touches, which this paper contributes and makes use of. This includes both the methods by which each component of the dataset was produced, and its exact contents.

A.1 Dataset content

For each object-grasp example in the dataset, the following are recorded:

- A dense point cloud of 10,000 points representing the object's surface, S^{obj}.
- Four local point clouds of at most 10,000 points, each representing the surface of the object at each touch site, $\{S_i^{loc}\}_{i=1}^4$.
- Four orthographic depth maps representing orthographic distance from the plane of the each touch sensor to any object geometry in front of them, $\{D_i\}_{i=1}^4$.
- Four simulated touch signals $T = [R_i, P_i, M_i]_{i=1}^{n_t=4}$, where R_i is one touch sensor reading, P_i its corresponding position and rotation in space, and M_i a binary mask indicating whether the touch is successful (i.e. the sensor is in contact with the object).
- Two vision signals V_u and V_o, corresponding to an image of the object alone (*unoccluded vision*) and an image of the object being grasped by the hand (*occluded vision*), respectively.

A.2 3D Objects and Hand

3D Objects: The 3D objects used for this dataset are from the 3D Warehouse data [1]. These are CAD objects and so possess geometry and texture information. For each object we want to grasp, S^{obj} is extracted from its surface using the technique defined in [58].

Hand: The Allegro hand [57] is used for grasping the objects. The URDF definition of this hand was altered to add the shape of a sensor to the finger tips and thumb tip of the hand. To make the hand easier to manipulate and render, its mesh components were altered by removing non-surface vertices and faces, and decimating the mesh. Note that this hand pre-processing has practically no impact on its behavior nor appearance.

A.3 Simulating Grasps

The 3D robotics simulator PyBullet [11] was used for producing the touch interactions. The process by which grasps are produced in PyBullet is displayed in Figure 11. First, the object and the Allegro hand are loaded into the simulator in a fixed pose (see first two images from left to right). The Allegro hand is then placed such that its palm is tangent to a random point on the object's surface (see third image). The distance from the object and the rotation of the hand on the tangent plane is also random. Using inverse kinematics, the joints of the hand are then rotated such that each of the hand's touch sensors meet the surface of the object, so long as physical integration of the hand and object allow it (see fourth image). This is repeated multiple times until sufficiently many grasps are recorded with

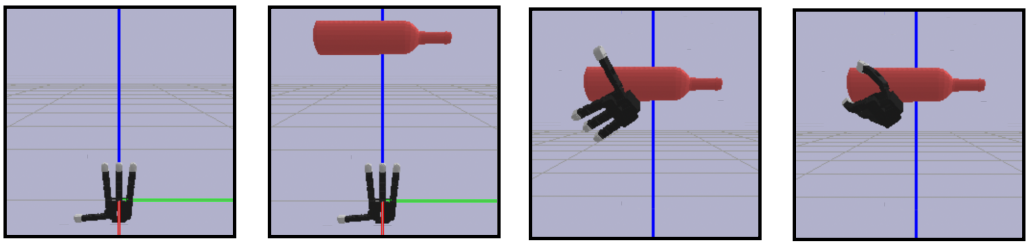


Figure 11: Visualization of the procedure used to create grasps in PyBullet.

successful touches. The pose information P_i, and the masks M_i from the best 5 grasps (with respect to the number of successful touches) are saved for use in the dataset.

A.4 Simulating Vision

To simulate the vision signals for each grasp, two RGB images V_u and V_o are rendered using Blender [10]. The object is placed at position [0, 0, 0.6] in its canonical 3D Warehouse pose, and the camera is placed at position [0.972, 0.461, 0.974], with rotation $[70.458°, 4.940°, 113.540°]$. Both images have resolution of $256 \times 256 \times 3$, and are produced with constant lighting from a single lamp.

A.5 Simulating Touch

For each grasp, to simulate the touch signal, T, at a successful touch site, and in particular its readings R_i, the 3D mesh of its corresponding object is first loaded into PyTorch [50]. Then, a 100×100 grid of points is created with the same size, position, shape, and orientation as the sensor. The dimensions of this grid define the resolution of the sensor: 100×100 pixels. The grid of points is projected orthogonally towards the surface of the object using sphere tracing, and so halts exactly at the touch site of the sensor. The distance these points move during this projection defines an orthographic depth map, D_i, for each touch sensor. The final position of the points defines the local structure of the surface, which the sensor interacts with. The depth maps of each touch site are saved, along with the points in the point cloud which correspond to depths smaller than the true depth of the sensor. We find the depth of the impression into the touch sensor as:

$$D_i' = ReLU(w - D_i), \tag{4}$$

where w is the depth of the sensor. Then, each position x, y in D_i' is projected into a 3D point cloud S_i^{loc} as follows: $[x/100, y/100, D_i'[x, y]]$.

To obtain the simulated RGB touch reading R_i from S_i^{loc}, three lights of pure red, green and blue are defined in a triangular shape above this surface at positions P_r, P_g, and P_b. We then use the Phong reflection model [52], where we assume zero specular or ambient lighting. The intensity values for the red colour channel of the simulated touch reading, $R_i \in \mathbb{R}^{100 \times 100 \times 3}$, are then defined as:

$$R_i = \lambda * \hat{n} * \hat{l}, \tag{5}$$

where λ is the diffuse reflection constant, $\hat{n}$ is the unit normal of the plane (broadcasted for shape compatibility), defined as

$$n = \left[-\frac{\mathrm{d}D_i'}{\mathrm{d}x}, -\frac{\mathrm{d}D_i'}{\mathrm{d}y}, 1 \right], \tag{6}$$

$$\hat{n} = \frac{n}{\|n\|}, \tag{7}$$

and $\hat{l}$ is the normalized light direction, defined as

$$\hat{l} = \frac{P_r - S_i^{loc}}{\|P_r - S_i^{loc}\|}, \tag{8}$$

where P_r is broadcast for shape compatibility. The intensity values for the green and blue colour channels are defined in the same manner.

Class	Objects	Grasps	Touches	% Successful
Bottle	487	2435	9740	71.8
Knife	416	2080	8320	54.1
Cellphone	493	2465	9860	67.2
Rifle	335	1675	6700	53.6

Table 4: Per-Class dataset statistics of the number of objects, grasps, touches and percentage of successful touches in each class.

A.6 Dataset Statistics

Five classes from 3D Warehouse were used in the dataset: the bottle, knife, cellphone, and rifle classes, for a total of 1731 objects. We split the dataset into a training set with 1298 objects, a validation set with 258 objects, and a test set with 175 objects. Statistics on the size, number of grasps, number of touches, and the percentage of those that were successful are provided in in Table 4. With respect to the distribution of successful touches over grasps, 9.47% of grasps possess only 1 successful touch, 26.08% possess 2, 53.83% possess 3, and finally 10.61% possess 4. Additional dataset examples are displayed in Figure 12.

B Local Touch Chart Predictions

In the following section, additional details are provided with respect to how predictions of local touch charts are created. These include details surrounding the architecture of models used, the range of hyperparameters considered, optimization details, additional results, runtime, and hardware used.

B.1 Model Architecture Details

To predict local charts we first predict a depth map. As described in the paper, a U-Net-based architecture [56] is leveraged for this task. The exact architecture for this network is displayed in Table 8.

B.2 Optimization Details

The model was trained using the Adam optimizer [38] with learning rate 5e-5 on 8 Tesla V100 GPUs with 16 CPU cores each, and batch size of 32. The learning rate for this experiment was tuned on the following grid [0.001, 0.0001, 0.00005, 0.00003, 0.00001]. The model was trained for a maximum number of 114 epochs (a total of 3 hours), it was evaluated every epoch on the validation set, and the best performing model across these evaluations was selected.

Moreover, it is worth noting that when optimizing the model's parameters, we compute the loss only for those positions in the touch sensor that interacted with the object. To do that, we first calculate the difference between the touch reading (sensor-object interaction) and an untouched sensor reading (no sensor-object interaction), and then compute the pixelwise ℓ_2^2 of the resulting differences. Finally, we apply a threshold of 0.001 and only consider those positions with a greater value.

B.3 Converting Point Clouds to Charts

As explained in the paper, the trained U-Net-based model produces a local point cloud for each touch signal in the dataset. Each point cloud is then used to produce a touch chart. To do this, a planar, triangular mesh with 81 vertices and 128 faces is first placed in the same position, orientation, shape, and size as the touch sensor which produced the touch signal. Then, using Adam[38] and learning rate 0.003, the position of the vertices in the chart is optimized so that it emulates the surface of the point cloud. The loss used for this optimization is the Chamfer distance between the point cloud and points uniformly sampled on the surface of the chart as in [59]. The optimization scheme halts when the loss is lower than 0.0006.

B.4 Additional Results

Additional visual reconstruction results are displayed in Figure 13. From these visualization, it can be seen that the predicted point clouds almost perfectly match the ground truth point clouds, though with a small degree of extrapolation beyond the observed surface. It can also be observed that the corresponding chart predictions almost perfectly match the predicted point clouds.

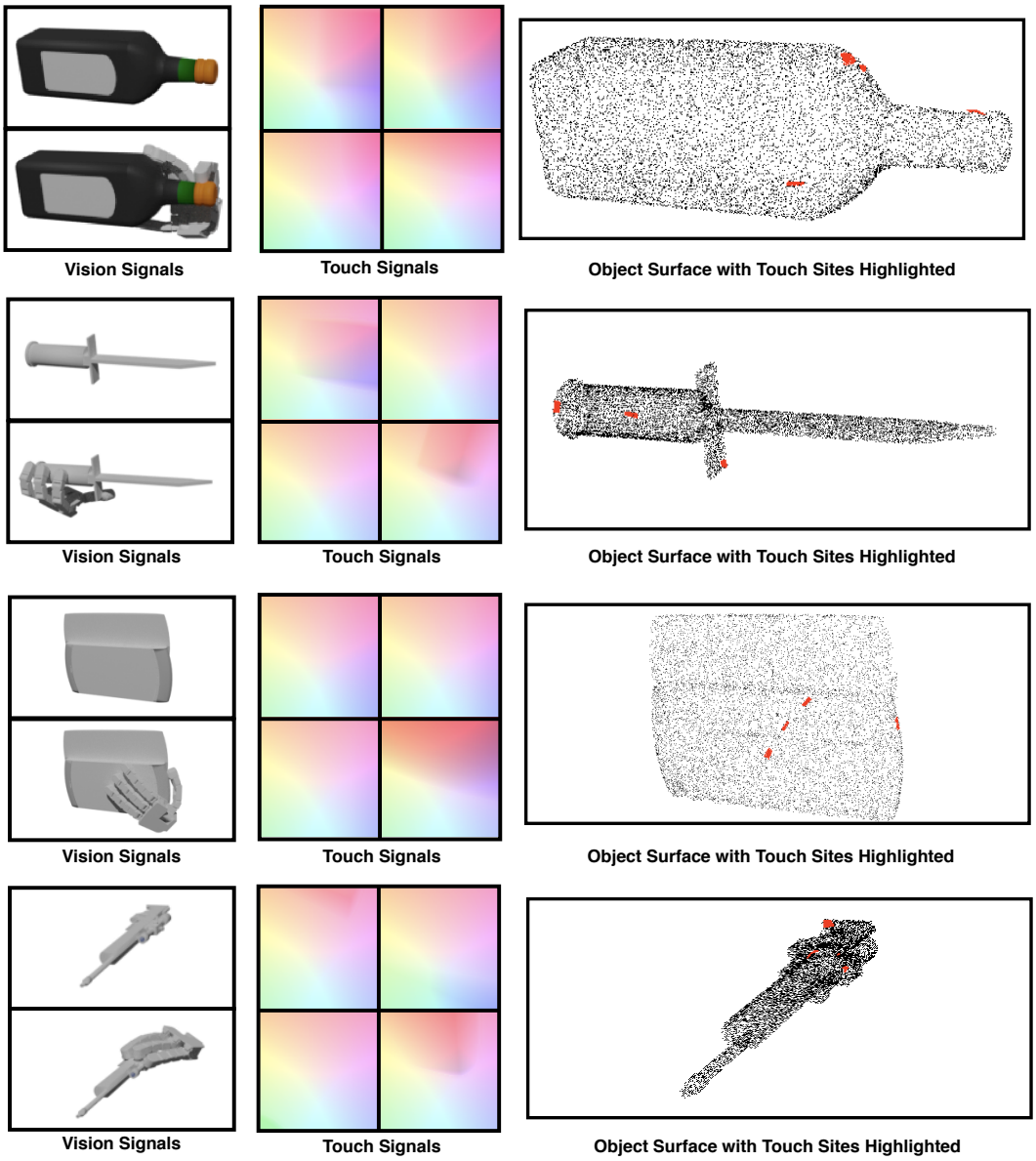


Figure 12: Visualization examples from the dataset showing an occluded (by hand) and unoccluded RGB image, 4 RGB images representing touch readings and a 3D object surface with touch sites highlighted.

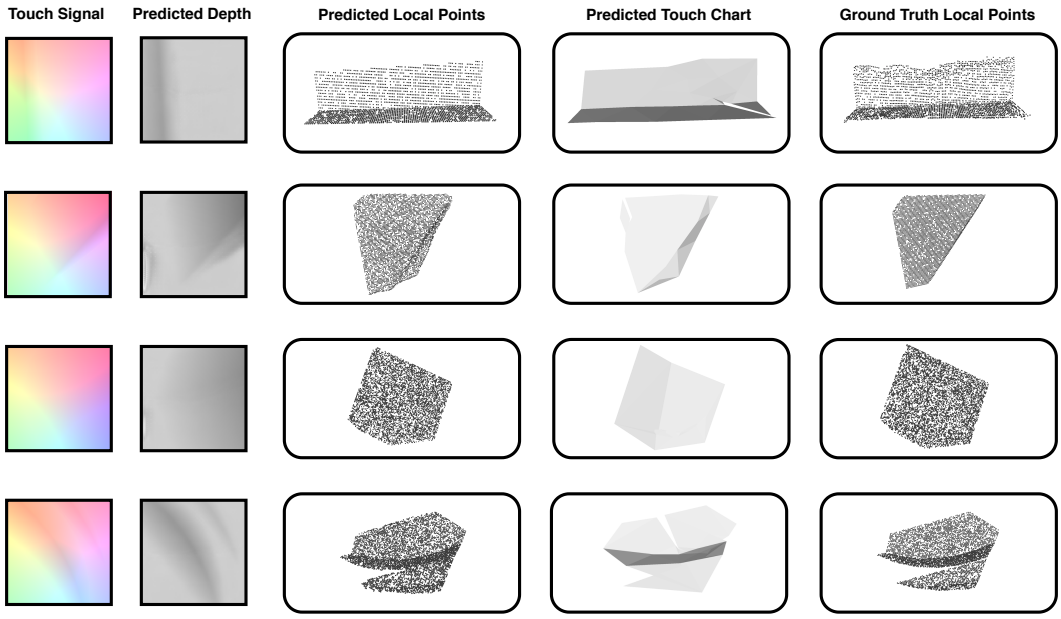


Figure 13: Local predictions of structure at each touch chart together with the corresponding charts produced from them.

C Global Vision Chart Predictions

In the following section, additional details are provided with respect to how vision charts are deformed around known touch charts, such that their combination emulates the target surface. These include details such as the models' architectures, the range of hyperparameters considered, optimization details, additional results, runtime, and hardware used.

C.1 Chart Feature Initialization

Vision and touch charts must have features defined over their vertices before they can be combined and passed to the Graph Convolutional Network (GCN) to be deformed. Three types of features are defined over all charts: image features, position of the vertex, and a masking feature indicating if the chart corresponds to a successful touch or not. For touch charts, the position and mask feature of each of their vertices are predefined. The initial position of vision charts is defined such that they combine to form a closed sphere, only touching at their boundary. This arrangement is highlighted in Figure 14. Their mask feature is set to 0 as they do not correspond to successful touches. The image features of both vision and touch charts are defined using perceptual feature pooling [67]. Here images are passed through a Convolutional Neural Network (CNN) and feature maps from intermediate layers are extracted. For any given vertex, its 3D position in space is projected onto the 2D plane of the input image using known camera parameters. The location of this projection in the pixel space of the image corresponds exactly to a position in each feature map. The vertex's image features are then defined as the bilinear interpolation between the four closest features to the projection in each feature map.

C.2 Model Architecture Details

Two networks are used to deform the positions of vision charts. The first is the CNN which defines image features for perceptual feature pooling, and the second is the GCN which updates the vertex positions. The network architectures for each model evaluated on the test set are displayed in Tables 10, 11, 12, 13, and 9. The GCN layers in each architecture are zero-neighbor layers as defined in [59].

C.3 Optimization Details

Each model type was trained using Adam [38] with learning rate 3e-5 and batch size 16 on a Tesla V100 GPU with 16 CPU cores. Each model was allowed to train for a maximum of 260 epoch (roughly 12 hours), was evaluated every epoch on the validation set and the best performing model across these evaluations was selected. Models were early-stopped if they failed to improve on the

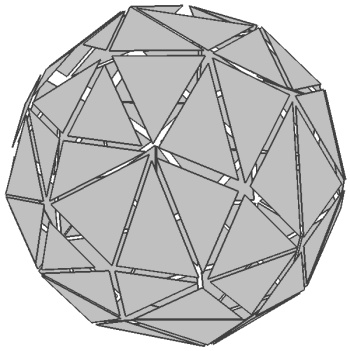


Figure 14: Initial positions of vision charts in a closed sphere. Charts have been separated slightly to improve their distinction.

Multiples of Touch Sensor Size	x1	x2	x3	x4	x5
Occluded Vision	6.687e-5	5.938e-5	5.305e-5	5.038e-5	4.841e-5
Occluded Vision + Touch	2.569e-5	2.970e-5	3.257e-5	3.393e-5	3.528e-5
Unoccluded Vision	4.553e-5	4.333e-5	4.080e-5	3.922e-5	3.866e-5
Unoccluded Vision + Touch	1.510e-5	1.944e-5	2.243e-5	2.494e-5	2.736e-5

Table 5: Local Chamfer distance in increasingly large square rings around each touch sites.

validation set for 70 epochs. The best performing model with occluded vision and touch was selected on epoch 113. The best performing model with only occluded vision was selected on epoch 114. The best performing model with unoccluded vision and touch was selected on epoch 122. The best performing model with only unoccluded vision was selected on epoch 99. The best performing model with only touch was selected on epoch 90.

C.4 Hyperparameter Details

The hyper-parameters tuned for the experiments in this setting were the learning rate, the number of layers in the CNN, the number of layers in the GCN, and the number of features per GCN layer. The possible settings for the learning rate were [1e-4, 3e-5, 1e-5]. The possible settings for the number of CNN layers were [12, 15, 18]. The possible settings for the number of GCN layers were [15, 20, 25]. The possible settings for the number of features per GCN layer were [150, 200, 250].

C.5 Additional Results

Additional reconstruction results for each class are visualized in Figure 15. Numerical results for the mutli-grasp experiment are displayed in Table 6. Numerical results for the experiment which examined the local Chamfer distance at expanding distances around each touch site are displayed in Table 5.

C.6 Single Image 3D Object Reconstruction

As mentioned in the main paper, and as a sanity check, the chart-based approach to 3D object reconstruction was also applied to the task of single image 3D object reconstruction to validate that it is competitive with other vision exclusive methods for 3D shape reconstruction. We used the 3D models with rendered images from [9], and compared using the evaluation setup released by [19].

Number of Grasps	1	2	3	4	5
Unoccluded Vision + Touch	0.804	0.714	0.689	0.695	0.654
Touch	3.05	1.769	1.479	1.296	1.237

Table 6: Chamfer distance when increasing the number of grasps provided to the models.

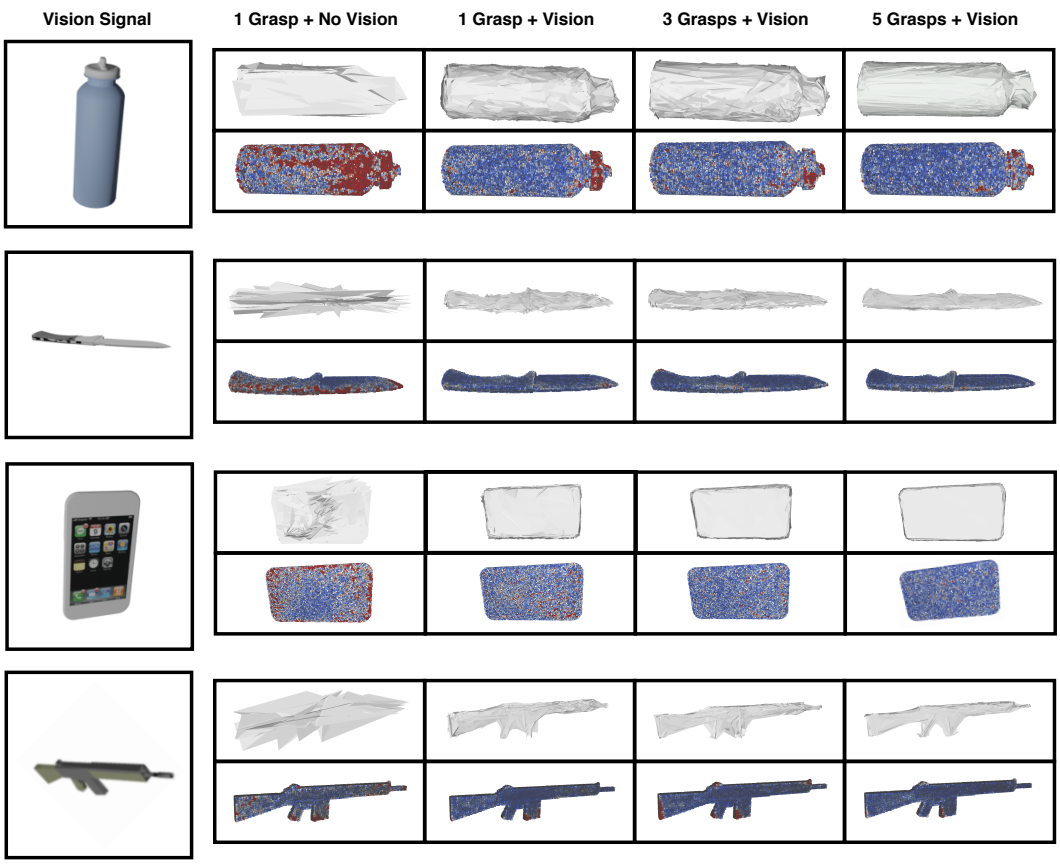


Figure 15: Reconstruction results of our method for each class across different input modalities and number of grasps. For vision signal, we use an unoccluded RGB image.

The model was trained for a maximum of 40 epochs (roughly 3 days of training), was evaluated after each epoch, and the best performing model across these evaluations was selected. The model was trained with the Adam optimizer [38] with learning rate e-5 and batch size 64 on a Tesla V100 GPU with 16 CPU cores. In this set up, we removed touch charts from our prediction pipeline and used exclusively vision signals. The architecture used for this experiment is displayed in Table 14.

We highlight the results of the evaluation in Table 7. The Chamfer Distance shown is the same metric as in the main paper, however, the scaling and density of points is different and so not comparable to other experiments. For a given distance threshold τ, $F1^{\tau}$ is the harmonic mean of the precision (percentage of predicted points with distance at most τ from any ground truth point) and recall (percentage of ground truth points with distance at most τ from any predicted point) of predicted and ground truth point clouds. The table demonstrates that we are competitive with other vision based approaches to 3D shape reconstruction, only failing to outperform the newly released MeshRCNN algorithm [19]. It should be noted that our approach has not been heavily tuned for this specific dataset or task, and so failing to overtake the most recent state of the art method is not wholly surprising.

	Chamfer Distance(↓)	$F1^{\tau}$ (↑)	$F1^{2\tau}$ (↑)
N3MR [36]	2.629	3.80	47.72
3D-R2N2 [9]	1.445	39.01	54.62
PSG [16]	0.593	48.58	69.78
MVD [58]	-	66.39	-
GEOMetrics [59]	-	67.37	-
Pixel2Mesh [67]	0.463	67.89	79.88
MeshRCNN [19] (Pretty)	0.391	69.83	81.76
MeshRCNN [19] (Best)	0.306	74.84	85.75
Ours	0.369	69.52	82.33

Table 7: Single image 3D shape reconstructing results on the 3D Warehouse Dataset. This evaluation is performed using the evaluation standard from [19] and [67].

Index	Input	Operation	Output Shape
(1)	Input	Conv (3×3) + BN + ReLU	$64 \times 100 \times 100$
(2)	(1)	Conv (3×3) + BN + ReLU	$64 \times 100 \times 100$
(3)	(2)	MaxPooling (2×2)	$64 \times 50 \times 50$
(4)	(3)	Conv (3×3) + BN + ReLU	$128 \times 50 \times 50$
(5)	(4)	Conv (3×3) + BN + ReLU	$128 \times 50 \times 50$
(6)	(5)	MaxPooling (2×2)	$128 \times 25 \times 25$
(7)	(6)	Conv (3×3) + BN + ReLU	$256 \times 25 \times 25$
(8)	(7)	Conv (3×3) + BN + ReLU	$256 \times 25 \times 25$
(9)	(8)	MaxPooling (2×2)	$256 \times 12 \times 12$
(10)	(8)	Conv (3×3) + BN + ReLU	$512 \times 12 \times 12$
(11)	(10)	Conv (3×3) + BN + ReLU	$512 \times 12 \times 12$
(12)	(11)	MaxPooling (2×2)	$512 \times 6 \times 6$
(13)	(12)	Conv (3×3) + BN + ReLU	$1024 \times 6 \times 6$
(14)	(13)	Conv (3×3) + BN + ReLU	$1024 \times 6 \times 6$
(15)	(14)	DeConv (2×2)	$512 \times 12 \times 12$
(16)	(15) (11)	Concatenate	$1024 \times 12 \times 12$
(17)	(16)	Conv (2×2) + BN + ReLU	$512 \times 12 \times 12$
(18)	(17)	DeConv (2×2)	$256 \times 25 \times 25$
(19)	(18) (8)	Concatenate	$512 \times 25 \times 25$
(20)	(19)	Conv (2×2) + BN + ReLU	$256 \times 25 \times 25$
(21)	(20)	DeConv (2×2)	$128 \times 50 \times 50$
(22)	(21) (5)	Concatenate	$256 \times 50 \times 50$
(23)	(22)	Conv (2×2) + BN + ReLU	$128 \times 50 \times 50$
(24)	(23)	DeConv (2×2)	$64 \times 100 \times 100$
(25)	(24) (2)	Concatenate	$128 \times 100 \times 100$
(26)	(25)	Conv (2×2) + BN + ReLU	$64 \times 100 \times 100$
(27)	(26)	Conv (1×1)	$1 \times 100 \times 100$

Table 8: Architecture for the U-Net style network used to predict point cloud positions for our local touch charts.

Index	Input	Operation	Output Shape
(1)	Vertex Inputs	GCN Layer	$\|V\| \times 250$
(2)	(1)	GCN Layer	$\|V\| \times 250$
...	...	...	...
(15)	(14)	GCN Layer	$\|V\| \times 3$

Table 9: Architecture for deforming charts with touch information only (|V|x3).

Index	Input	Operation	Output Shape
(1)	Image Input	Conv (3×3) + BN + ReLU	$16 \times 127 \times 127$
(2)	(1)	Conv (3×3) + BN + ReLU	$16 \times 125 \times 125$
(3)	(2)	Conv (3×3) + BN + ReLU	$16 \times 123 \times 123$
(4)	(3)	Conv (3×3) + BN + ReLU	$16 \times 121 \times 121$
(5)	(4)	Conv (3×3) + BN + ReLU	$16 \times 119 \times 119$
(6)	(5)	Conv (3×3) (stride 2) + BN + ReLU	$32 \times 59 \times 59$
(7)	(6)	Conv (3×3) + BN + ReLU	$32 \times 57 \times 57$
(8)	(7)	Conv (3×3) + BN + ReLU	$32 \times 55 \times 55$
(9)	(8)	Conv (3×3) + BN + ReLU	$32 \times 53 \times 53$
(10)	(9)	Conv (3×3) + BN + ReLU	$32 \times 51 \times 51$
(11)	(10)	Conv (3×3) (stride 2) + BN + ReLU	$64 \times 25 \times 25$
(12)	(11)	Conv (3×3) + BN + ReLU	$64 \times 23 \times 23$
(13)	(12)	Conv (3×3) + BN + ReLU	$64 \times 21 \times 21$
(14)	(13)	Conv (3×3) + BN + ReLU	$64 \times 19 \times 19$
(15)	(14)	Conv (3×3) + BN + ReLU	$64 \times 17 \times 17$
(16)	(15)	Conv (3×3) (stride 2) + BN + ReLU	$128 \times 8 \times 8$
(17)	(16)	Conv (3×3) + BN + ReLU	$128 \times 6 \times 6$
(18)	(17)	Conv (3×3) + BN + ReLU	$128 \times 4 \times 4$
(19)	(10) (15) (18)	perceptual feature pooling	$\|V\| \times 224$
(20)	(19) Vertex Input	Concatenate	$\|V\| \times 228$
(21)	(20)	GCN Layer	$\|V\| \times 250$
(22)	(21)	GCN Layer	$\|V\| \times 250$
...	...	...	...
(41)	(40)	GCN Layer	$\|V\| \times 3$

Table 10: Architecture for deforming charts with occluded vision signals and touch information. The input to this model is an RGB image (4x256x256), and vertex features (|V|x4). BN refers to batch normalization.

Index	Input	Operation	Output Shape
(1)	Image Input	Conv (3×3) + BN + ReLU	$16 \times 127 \times 127$
(2)	(1)	Conv (3×3) + BN + ReLU	$16 \times 125 \times 125$
(3)	(2)	Conv (3×3) + BN + ReLU	$16 \times 123 \times 123$
(4)	(3)	Conv (3×3) + BN + ReLU	$16 \times 121 \times 121$
(5)	(4)	Conv (3×3) + BN + ReLU	$16 \times 119 \times 119$
(6)	(5)	Conv (3×3) (stride 2) + BN + ReLU	$32 \times 59 \times 59$
(7)	(6)	Conv (3×3) + BN + ReLU	$32 \times 57 \times 57$
(8)	(7)	Conv (3×3) + BN + ReLU	$32 \times 55 \times 55$
(9)	(8)	Conv (3×3) + BN + ReLU	$32 \times 53 \times 53$
(10)	(9)	Conv (3×3) + BN + ReLU	$32 \times 51 \times 51$
(11)	(10)	Conv (3×3) (stride 2) + BN + ReLU	$64 \times 25 \times 25$
(12)	(11)	Conv (3×3) + BN + ReLU	$64 \times 23 \times 23$
(13)	(12)	Conv (3×3) + BN + ReLU	$64 \times 21 \times 21$
(14)	(13)	Conv (3×3) + BN + ReLU	$64 \times 19 \times 19$
(15)	(14)	Conv (3×3) + BN + ReLU	$64 \times 17 \times 17$
(16)	(15)	Conv (3×3) (stride 2) + BN + ReLU	$128 \times 8 \times 8$
(17)	(16)	Conv (3×3) + BN + ReLU	$128 \times 6 \times 6$
(18)	(17)	Conv (3×3) + BN + ReLU	$128 \times 4 \times 4$
(19)	(10) (15) (18)	perceptual feature pooling	$\|V\| \times 224$
(20)	(19) Vertex Input	Concatenate	$\|V\| \times 227$
(21)	(20)	GCN Layer	$\|V\| \times 200$
(22)	(21)	GCN Layer	$\|V\| \times 200$
...	...	...	...
(41)	(40)	GCN Layer	$\|V\| \times 3$

Table 11: Architecture for deforming charts with occluded vision signals without touch information. The input to this model is an RGB image (4x256x256), and vertex features (|V|x3). BN refers to batch normalization.

Index	Input	Operation	Output Shape
(1)	Image Input	Conv (3×3) + BN + ReLU	$16 \times 127 \times 127$
(2)	(1)	Conv (3×3) + BN + ReLU	$16 \times 125 \times 125$
(3)	(2)	Conv (3×3) + BN + ReLU	$16 \times 123 \times 123$
(4)	(3)	Conv (3×3) + BN + ReLU	$16 \times 121 \times 121$
(5)	(4)	Conv (3×3) + BN + ReLU	$16 \times 119 \times 119$
(6)	(5)	Conv (3×3) (stride 2) + BN + ReLU	$32 \times 59 \times 59$
(7)	(6)	Conv (3×3) + BN + ReLU	$32 \times 57 \times 57$
(8)	(7)	Conv (3×3) + BN + ReLU	$32 \times 55 \times 55$
(9)	(8)	Conv (3×3) + BN + ReLU	$32 \times 53 \times 53$
(10)	(9)	Conv (3×3) + BN + ReLU	$32 \times 51 \times 51$
(11)	(10)	Conv (3×3) (stride 2) + BN + ReLU	$64 \times 25 \times 25$
(12)	(11)	Conv (3×3) + BN + ReLU	$64 \times 23 \times 23$
(13)	(12)	Conv (3×3) + BN + ReLU	$64 \times 21 \times 21$
(14)	(13)	Conv (3×3) + BN + ReLU	$64 \times 19 \times 19$
(15)	(14)	Conv (3×3) + BN + ReLU	$64 \times 17 \times 17$
(16)	(15)	Conv (3×3) (stride 2) + BN + ReLU	$128 \times 8 \times 8$
(17)	(16)	Conv (3×3) + BN + ReLU	$128 \times 6 \times 6$
(18)	(17)	Conv (3×3) + BN + ReLU	$128 \times 4 \times 4$
(19)	(10) (15) (18)	perceptual feature pooling	$\|V\| \times 224$
(20)	(19) Vertex Input	Concatenate	$\|V\| \times 228$
(21)	(20)	GCN Layer	$\|V\| \times 200$
(22)	(21)	GCN Layer	$\|V\| \times 200$
...	...	...	...
(46)	(45)	GCN Layer	$\|V\| \times 3$

Table 12: Architecture for deforming charts with unoccluded vision signals and touch information. The input to this model is an RGB image (4x256x256), and vertex features (|V|x4). BN refers to batch normalization.

Index	Input	Operation	Output Shape
(1)	Image Input	Conv (3×3) + BN + ReLU	$16 \times 127 \times 127$
(2)	(1)	Conv (3×3) + BN + ReLU	$16 \times 125 \times 125$
(3)	(2)	Conv (3×3) + BN + ReLU	$16 \times 123 \times 123$
(4)	(3)	Conv (3×3) (stride 2) + BN + ReLU	$32 \times 61 \times 61$
(5)	(4)	Conv (3×3) + BN + ReLU	$32 \times 59 \times 59$
(6)	(5)	Conv (3×3) + BN + ReLU	$32 \times 57 \times 57$
(7)	(6)	Conv (3×3) (stride 2) + BN + ReLU	$64 \times 28 \times 28$
(8)	(7)	Conv (3×3) + BN + ReLU	$64 \times 26 \times 26$
(9)	(8)	Conv (3×3) + BN + ReLU	$64 \times 24 \times 24$
(10)	(9)	Conv (3×3) (stride 2) + BN + ReLU	$128 \times 11 \times 11$
(11)	(10)	Conv (3×3) + BN + ReLU	$128 \times 9 \times 9$
(12)	(11)	Conv (3×3) + BN + ReLU	$128 \times 7 \times 7$
(13)	(3) (6) (9) (11)	perceptual feature pooling	$\|V\| \times 240$
(14)	(13) Vertex Input	Concatenate	$\|V\| \times 243$
(15)	(14)	GCN Layer	$\|V\| \times 250$
(16)	(15)	GCN Layer	$\|V\| \times 250$
...	...	...	...
(35)	(34)	GCN Layer	$\|V\| \times 3$

Table 13: Architecture for deforming charts with unoccluded vision signals without touch information. The input to this model is an RGB image (4x256x256), and vertex features (|V|x3). BN refers to batch normalization.

Index	Input	Operation	Output Shape
(1)	Image Input	Conv (3×3) + IN + ReLU	$16 \times 69 \times 69$
(2)	(1)	Conv (3×3) + IN + ReLU	$16 \times 69 \times 69$
(3)	(2)	Conv (3×3) + IN + ReLU	$16 \times 69 \times 69$
(4)	(3)	Conv (3×3) + IN + ReLU	$16 \times 69 \times 69$
(5)	(4)	Conv (3×3) + IN + ReLU	$16 \times 69 \times 69$
(6)	(5)	Conv (3×3) (stride 2) + IN + ReLU	$32 \times 35 \times 35$
(7)	(6)	Conv (3×3) + IN + ReLU	$32 \times 35 \times 35$
(8)	(7)	Conv (3×3) + IN + ReLU	$32 \times 35 \times 35$
(9)	(8)	Conv (3×3) + IN + ReLU	$32 \times 35 \times 35$
(10)	(9)	Conv (3×3) + IN + ReLU	$32 \times 35 \times 35$
(11)	(10)	Conv (3×3) (stride 2) + IN + ReLU	$64 \times 18 \times 18$
(12)	(11)	Conv (3×3) + IN + ReLU	$64 \times 18 \times 18$
(13)	(12)	Conv (3×3) + IN + ReLU	$64 \times 18 \times 18$
(14)	(13)	Conv (3×3) + IN + ReLU	$64 \times 18 \times 18$
(15)	(14)	Conv (3×3) + IN + ReLU	$64 \times 18 \times 18$
(16)	(15)	Conv (3×3) (stride 2) + IN + ReLU	$128 \times 9 \times 9$
(17)	(16)	Conv (3×3) + IN + ReLU	$128 \times 9 \times 9$
(18)	(17)	Conv (3×3) + IN + ReLU	$128 \times 9 \times 9$
(19)	(18)	Conv (3×3) + IN + ReLU	$128 \times 9 \times 9$
(20)	(19)	Conv (3×3) + IN + ReLU	$128 \times 9 \times 9$
(21)	(20)	Conv (3×3) (stride 2) + IN + ReLU	$256 \times 5 \times 5$
(22)	(21)	Conv (3×3) + IN + ReLU	$256 \times 5 \times 5$
(23)	(22)	Conv (3×3) + IN + ReLU	$256 \times 5 \times 5$
(24)	(23)	Conv (3×3) + IN + ReLU	$256 \times 5 \times 5$
(25)	(24)	Conv (3×3) + IN + ReLU	$256 \times 5 \times 5$
(26)	(25) (22) (19)	perceptual feature pooling	$\|V\| \times 896$
(27)	(26)	Linear + ReLU	$\|V\| \times 250$
(28)	(27) Vertex Input	Concatenate	$\|V\| \times 253$
(29)	(28)	GCN Layer	$\|V\| \times 250$
(30)	(29)	GCN Layer	$\|V\| \times 250$
...	...	...	...
(53)	(52)	GCN Layer	$\|V\| \times 3$

Table 14: Architecture for chart deformation in the single image 3D object reconstruction experiment on the 3D Warehouse. The input to this model is an RGB image (3x256x256), and vertex features (|V|x3). IN refers to instance normalization [65].